Unconventional Dirac-Weyl semimetal with ultralong surface arc in phononic crystals

Peng Wu, Feng Gao, Xiao Xiang, Chen Zheng, Yu-Gui Peng,* and Xue-Feng Zhu†
School of Physics and Innovation Institute, Huazhong University of Science and Technology, Wuhan 430074, China

(Received 3 May 2024; revised 9 July 2024; accepted 26 July 2024; published 12 September 2024)

The fascinating properties of unconventional Dirac and Weyl nodes in crystalline systems, carrying a topological charge of ±2, have captured the attention of researchers. Here, applying $k \cdot p$ analysis, we demonstrate that space group 92 facilitates the emergence of charge-2 Dirac point and charge-2 Weyl point. Notably, the constructed phononic crystal is allowed to be a concise configuration containing only a charge-2 Dirac point and a charge-2 Weyl point in pairs appearing simultaneously, that is, the realization of the unconventional Dirac-Weyl semimetal (UDWS). The projected dispersion bands reveal the unique double helical surface arcs of UDWS, which alternate from the projected charge-2 Dirac point to the projected charge-2 Weyl point, spanning the entire Brillouin zone with ultralong trajectories. The unique global surface arc characteristic demonstrates robust resilience against defects, underscoring its suitability as an optimal platform for investigating ultralong surface arcs.

DOI: 10.1103/PhysRevB.110.094104

I. INTRODUCTION

The Weyl point (WP) [1–7] is characterized by an isolated linear crossing point in momentum space, exhibiting a magnetic monopole in the Berry curvature field and described by a topological charge of ±1 (or chiral). The presence of a nonzero topological charge gives rise to intriguing transport phenomena, including the negative magnetoresistance effect [8,9], chiral anomaly [10–12], nonlocal transport [13], and chiral gauge anomaly [14]. The WP, known for its remarkable stability requiring only translational symmetry, can only be annihilated by merging two WPs with opposite charges appearing at the same momentum position, culminating in a Dirac point (DP) [15–21] with a fourfold linear degeneracy and zero topological charge. This DP, akin to the three-dimensional analog of graphene [22,23], exhibit the properties of ultrahigh mobility and giant magnetoresistance [24], sparking a continuous research wave. In contrast to elementary particles adhering to Poincaré symmetry in nature, quasiparticles in crystal systems must adhere to additional constraints imposed by space group symmetries. Given the multitude of space group symmetries, many novel quasiparticles are allowed to appear in crystal systems, such as charge-2 WP [25,26], triple point [27–31], charge-2 DP [32–34], sixfold point [35–37], nodal line [38–42], and nodal surfaces [43–46]. Among them, the charge-2 WP and charge-2 DP, commonly referred to as "double Weyl nodes," are two notable members that undoubtedly attract substantial scrutiny due to their high topological charges of ±2.

Benefiting from the insights of topological matters in solid systems, various acoustic analogs in phononic crystals [47–50] have been extensively explored, encompassing Chern insulator [51], spin Chern insulator [52,53], quadrupole topological insulator [54,55], charge-2 Weyl semimetal [56,57], charge-2 Dirac semimetal [58], and several higher-order topological states [59–62]. The superior macroscopic controllability and manufacturability of phononic crystals, in comparison to the complex manipulations required at the atomic scale in electronic materials, provide an elegant framework to easily probe the topological matters. These numerous distinctive acoustic transmission properties, such as one-way transport [51,53], negative refraction [63–65], zero refraction index [49,66], and topological pumping phenomenon [67] arising from synthetic spaces, hold great promise for waveguide design and acoustic processing. Also, captivating transport phenomena have inspired intense debates in the photonic crystal field [68–70], introducing novel aspects of the quantized circular photogalvanic effect [71], and unconventional photocurrents [72]. In general, DPs typically appear at the time-reversal invariant points, requiring an environment where both space inversion symmetry (P) and time reversion symmetry ($\mathcal{T}$) are preserved. Conversely, WPs merge in pairs when either P symmetry or $\mathcal{T}$ symmetry is broken. Initially, the coexistence of DPs and WPs may seem to be incompatible due to their distinct symmetry requirements. However, recent research exceeds this limitation by revealing that the preservation of P symmetry is not a prerequisite for DP formation, allowing nonsymmorphic symmetry to replace it [73]. Plus, multiple appearances of degenerate points on the high symmetry lines provide another plausible pathway to DP formation [74]. This new understanding allows for simultaneous presence of DPs and WPs in a system, termed as Dirac-Weyl semimetals (DWSs) [75]. The symmetry conditions for DWSs have been systematically proposed based on symmetry constraints by Ref. [73] and the electronic material of SrHgPb [76] is later identified as a DWS. Further, the scope of DWSs extends to other types of nodes in coexistence systems, including DPs and Weyl nodal line system [77], WPs

*Contact author: ygpeng@hust.edu.cn
†Contact author: xfzhu@hust.edu.cn

and Dirac nodal lines system [78], Dirac and Weyl nodal rings system [79], Dirac nodal line and nodal surfaces system [80], and even scenarios involving WPs in a higher-order topological Dirac semimetal [81] that continue to stimulate intense discussions. It is crucial to note that the coexistence of DPs and WPs in the DWSs system mentioned above merely represent the concurrent presence of two types of nodes without establishing a direct correlation between them. This limitation is regrettable as a genuine significant coexistence of the two could enhance the topological properties of these entities and potentially lead to the emergence of novel topological phenomena. Fortunately, a three-terminal Weyl system, as observed in phononic crystals [57] and topological phononic materials [82], demonstrates a "real" connection for the coexistence of charge-2 WPs and conventional WPs. However, it is lacking for the realization of unconventional Dirac-Weyl semimetals (UDWSs) containing the charge-2 DPs and the charge-2 WPs in the acoustic system and exploring the "real" connections therein.

In this paper, we perform a symmetry analysis to validate the feasibility of UDWS within space group (SG) 92. Notably, the symmetry constraints determine the precise locations for the charge-2 DP positioned at A and the charge-2 WP situated at Γ. We construct a phononic crystal and confirm the dispersion bands, which illustrate the presence of a distinct nodal distribution pattern. This feature highlights the connectivity of the unique double helical surface arc linking the projection points of the charge-2 DP and the charge-2 WP, with extensions reaching into the neighboring Brillouin zone (BZ), showcasing characteristics of remarkable ultralong behavior. The examination of the acoustic pressure field distribution of the defective structures highlight its outstanding robustness, indicating the substantial potential of UDWS for advancing acoustic device applications in signal processing and low-less communication.

II. SYMMETRY ANALYSIS

For a charge-2 DP to exist, the required symmetry is the space point group of D_2, D_4, or T symmetry equipped with a screw axis, which necessitates C_3, C_4, or C_6 symmetry for the charge-2 WP to be present [83]. In contrast to a system with multiple DPs and WPs, the generation of numerous indistinguishable surface arcs pose a formidable challenge for observing and confirming their topological properties. Hence we focus on a concise case of both these nodes existing at high symmetry points, as SG 92 ($P4_12_12$) is suitable. In detail, the charge-2 DP resides on the boundary of the BZ at A with momentum position $(\frac{1}{2}, \frac{1}{2}, \frac{1}{2})$, while the charge-2 WP is situated at the center of the BZ at Γ with momentum position (0,0,0). To begin our analysis, we first examine the charge-2 DP at A. The space group 92 is characterized by three generators: $\widetilde{C}_{4z} \equiv \{C_{4z}|00\frac{1}{4}\}$, $\widetilde{C}_{2x} \equiv \{C_{2x}|\frac{1}{2}\frac{1}{2}0\}$, and time reversal symmetry $\mathcal{T}$. The operations applied to the lattice result in changing the lattice coordinates as follows:

$$\begin{aligned}\widetilde{C}_{4z} &: (x, y, z) \to \left(y, -x, z + \tfrac{1}{4}\right),\\ \widetilde{C}_{2x} &: (x, y, z) \to \left(x + \tfrac{1}{2}, -y + \tfrac{1}{2}, -z\right).\end{aligned} \tag{1}$$

At the high symmetry point A, we have

$$\widetilde{C}_{4z}^4 = T_{001} = -1, \tag{2}$$

$$C_{2x}^2 = T_{100} = -1, \tag{3}$$

$$\widetilde{C}_{4z}\widetilde{C}_{2x} = T_{0\bar{1}1}\widetilde{C}_{2x}\widetilde{C}_{4z}^3 = \widetilde{C}_{2x}\widetilde{C}_{4z}^3, \tag{4}$$

where T_r is used to describe the direction and length of the translation vector. The eigenvalues of $\widetilde{C}_{4z}$ that can be obtained from Eq. (2) are one of the sets $\{\pm e^{i\pi/4}, \pm e^{-i\pi/4}\}$. We define $|u_k\rangle$ as the eigenstate of the Hamiltonian H with the eigenvalue E. Given the $[\widetilde{C}_{4z}, H] = 0$ relation, the $\widetilde{C}_{4z}$ and H have the same eigenstate and a corresponding eigenvalue of $e^{i\pi/4}$, namely,

$$\widetilde{C}_{4z}|u_k\rangle = e^{i\pi/4}|u_k\rangle. \tag{5}$$

By combining Eqs. (2)–(5), we have

$$\begin{aligned}\widetilde{C}_{4z}\widetilde{C}_{2x}|u_k\rangle &= \widetilde{C}_{2x}\widetilde{C}_{4z}^3|u_k\rangle = e^{i3\pi/4}\widetilde{C}_{2x}|u_k\rangle,\\ \widetilde{C}_{4z}\mathcal{T}|u_k\rangle &= \mathcal{T}\widetilde{C}_{4z}|u_k\rangle = e^{-i\pi/4}\mathcal{T}|u_k\rangle,\\ \widetilde{C}_{4z}\widetilde{C}_{2x}\mathcal{T}|u_k\rangle &= \widetilde{C}_{2x}\mathcal{T}\widetilde{C}_{4z}^3|u_k\rangle = e^{-i3\pi/4}\mathcal{T}|u_k\rangle,\end{aligned} \tag{6}$$

which give a set of linearly independent states $\{|u_k\rangle, \mathcal{T}|u_k\rangle, \widetilde{C}_{2x}\mathcal{T}|u_k\rangle, \widetilde{C}_{2x}|u_k\rangle\}$, plus the fact that the four states with equal eigenvalues are quickly noticeable. Based on the above four eigenstates, the representation matrices for $\widetilde{C}_{4z} \equiv \{C_{4z}|00\frac{1}{4}\}$, $\widetilde{C}_{2x} \equiv \{C_{2x}|\frac{1}{2}\frac{1}{2}0\}$, and $\mathcal{T}$ can be written as

$$\begin{aligned}\widetilde{C}_{4z} &= \begin{pmatrix} e^{i\pi/4} & 0 & 0 & 0\\ 0 & e^{-i\pi/4} & 0 & 0\\ 0 & 0 & e^{-3i\pi/4} & 0\\ 0 & 0 & 0 & e^{3i\pi/4}\end{pmatrix},\\ \widetilde{C}_{2x} &= \begin{pmatrix} 0 & 0 & 0 & -1\\ 0 & 0 & -1 & 0\\ 0 & 1 & 0 & 0\\ 1 & 0 & 0 & 0\end{pmatrix} = -i\sigma_y \otimes \sigma_x,\\ D(\mathcal{T}) &= \begin{pmatrix} 0 & 1 & 0 & 0\\ 1 & 0 & 0 & 0\\ 0 & 0 & 0 & 1\\ 0 & 0 & 1 & 0\end{pmatrix}\mathcal{K} = \sigma_0 \otimes \sigma_x\mathcal{K},\end{aligned} \tag{7}$$

where σ_i, τ_j are Pauli matrices, $\Gamma_{i,j} = \sigma_i \otimes \tau_j$, and $\mathcal{K}$ is the complex conjugate operator. Under the constraints from the symmetries, the effective model satisfies

$$\begin{aligned}D(\widetilde{C}_{4z})\mathcal{H}_{\text{eff}}(\mathbf{k})D^{-1}(\widetilde{C}_{4z}) &= \mathcal{H}_{\text{eff}}(k_y, -k_x, k_z),\\ D(\widetilde{C}_{2x})\mathcal{H}_{\text{eff}}(\mathbf{k})D^{-1}(\widetilde{C}_{2x}) &= \mathcal{H}_{\text{eff}}(k_x, -k_y, -k_z),\\ D(\mathcal{T})\mathcal{H}_{\text{eff}}(\mathbf{k})D^{-1}(\mathcal{T}) &= \mathcal{H}_{\text{eff}}(-k_x, -k_y, -k_z).\end{aligned} \tag{8}$$

According to Eq. (8), we can then construct the $k \cdot p$ model around Γ point

$$\begin{aligned}\mathcal{H}_{\text{eff}}(\mathbf{k}) &= \begin{pmatrix} ak_z & 0 & 0 & -imk_+\\ 0 & -ak_z & -imk_- & 0\\ 0 & imk_+ & ak_z & 0\\ imk_- & 0 & 0 & -ak_z\end{pmatrix}\\ &= ak_z\Gamma_{0z} + mk_x\Gamma_{yx} - mk_y\Gamma_{yy},\end{aligned} \tag{9}$$

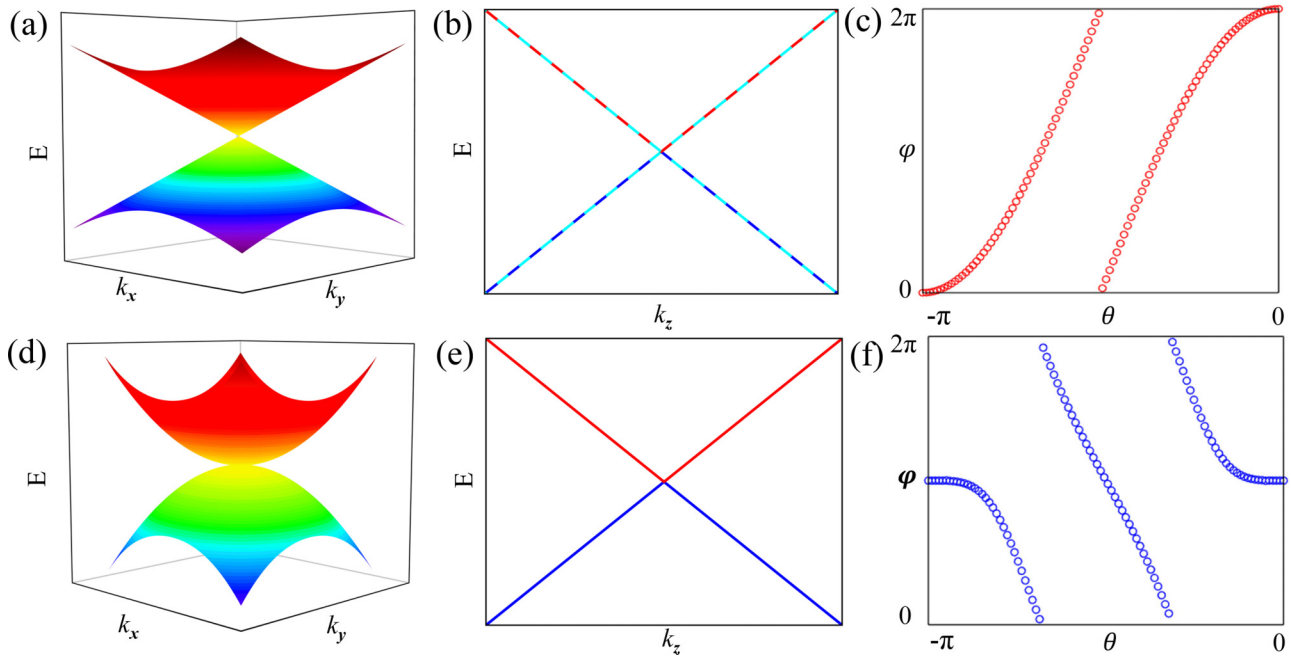

FIG. 1. 3D bulk band dispersions by $k \cdot p$ method in the k_x-k_y plane [along the k_z line] for (a) [(b)] a charge-2 DP and (d) [(e)] a charge-2 WP. The evolution of Wannier charge centers (WCCs) for (c) a charge-2 DP (with topological charge $= -2$) and (f) a charge-2 WP (with topological charge $= +2$).

where a and m are nonzero real parameters and $k_\pm = k_x \pm k_y$. The Hamiltonian exhibits a fourfold degeneracy at $\mathbf{k} = 0$ and linear dispersion when $\mathbf{k} \to 0$.

The charge-2 WP emerge at Γ hosting the little group D_4, which has a two-dimensional irreducible representation corresponding to doubly degenerate nodes. The basis functions of the generator are $\{S_x, S_y\}$ and the matrix can be expressed as

$$\begin{aligned} D(\widetilde{C}_{4z}) &= \begin{pmatrix} 0 & -1 \\ 1 & 0 \end{pmatrix} = i\sigma_y, \\ D(\widetilde{C}_{2x}) &= \begin{pmatrix} 1 & 0 \\ 0 & -1 \end{pmatrix} = \sigma_z, \\ D(\mathcal{T}) &= \begin{pmatrix} -1 & 0 \\ 0 & -1 \end{pmatrix} \mathcal{K} = \sigma_0 \mathcal{K}. \end{aligned} \tag{10}$$

Thus one can obtain the effective Hamiltonian of the two bands as

$$\begin{aligned} \mathcal{H}_{\text{eff}}(\mathbf{k}) &= \begin{pmatrix} a_1\left(k_x^2 - k_y^2\right) & a_2 k_x k_y - i a_3 k_z \\ a_2 k_x k_y + i a_3 k_z & a_1\left(k_y^2 - k_x^2\right) \end{pmatrix} \\ &= a_1\left(k_x^2 - k_y^2\right)\sigma_z + a_2 k_x k_y \sigma_x + a_3 k_z \sigma_y, \end{aligned} \tag{11}$$

where $a_{1,2,3}$ are real parameters. The Hamiltonian exhibits the quasiparticle excitation around the Γ point with linear dispersion along the k_z axis and quadratic dispersion in the k_x-k_y plane, agreeing with the behavior of a charge-2 WP.

Using the $k \cdot p$ effective model Hamiltonian by Eq. (8), we present the bulk dispersion in the k_x-k_y plane and along the high symmetry line k_z for a fourfold degenerate DP in Figs. 1(a) and 1(b), showcasing its linear dispersion in all directions. Likewise, the dispersion of a twofold degenerate WP is depicted in Figs. 1(d) and 1(e) based on Eq. (11), featuring quadratic dispersion in the k_x-k_y plane and linear dispersion along the k_z axis. To ascertain the topological characteristics of the two nodes, we utilize the Wilson loop approach [84,85] to visually identify that the topological charges of a fourfold degenerate point at A are -2 and topological charges of the twofold degenerate point at Γ are $+2$, as depicted in Figs. 1(c) and 1(f), consistent with our analysis of the $k \cdot p$ method.

III. RESULTS AND DISCUSSION

To further investigate the topological behavior of UDWS in acoustics, we design a model of a phononic crystal, shown in Fig. 2(a). The unit cell structure is composed of four block layers (viz., L1, L2, L3, L4), with cylinders connecting the adjacent layers in the vertical direction. The planer view of each layer is illustrated in Fig. 2(c); one can clearly observe that the $\widetilde{C}_{4z} \equiv \{C_{4z}|00\frac{1}{4}\}$ symmetry is fulfilled, i.e., after applying $\widetilde{C}_{4z}$, an exchange of the layer sequence L1 → L2 → L3 → L4 follows. The other generating element, screw rotation operation $\widetilde{C}_{2x} \equiv \{C_{2x}|\frac{1}{2}\frac{1}{2}0\}$, can be decomposed into two successive operations of a rotation $\{C_{2x}|000\}$ and a translation $\{T_r|\frac{1}{2}\frac{1}{2}0\}$. To visualize the results from the operations $\{C_{2x}|000\}$ and $\{T_r|\frac{1}{2}\frac{1}{2}0\}$, we draw 2×2 cells with layer number L2, as shown in the left panel of Fig. 2(b), where the deep brown cell is the primary focus of our demonstration. When the rotation axis $\{C_{2x}|000\}$ is introduced, the second block layer L2 [the left one in Fig. 2(b)] can be transformed into the middle one in Fig. 2(b) and further transformed into the right one in Fig. 2(b) after the translation operation $\{T_r|\frac{1}{2}\frac{1}{2}0\}$. Since the operation $\{C_{2x}|000\}$ swaps z for $-z$, the block layers transform from L2 to L3. The above operations show that the layers L2 and L3 can be related by using the generating-element operation $\widetilde{C}_{2x}$, that is, our model obeys the symmetry $\widetilde{C}_{2x}$.

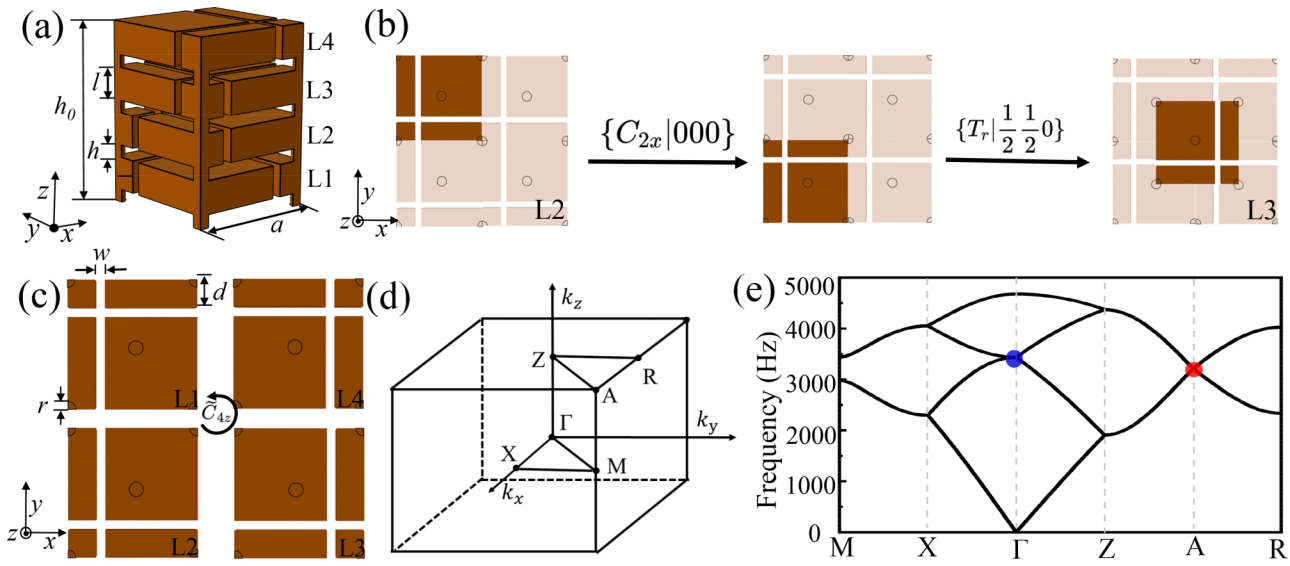

FIG. 2. Unit cell for the designed phononic crystal. The brown regions represent the air cavities and coupling tubes with rigid boundaries. The unit cell is composed of four block layers, labeled with L1, L2, L3, L4, and the cylindrical tubes are coupling ones that connect the four layers. (b) A step-by-step schematic of the layer structure (L2 and L3) with $\widetilde{C}_{2x}$ symmetry. (c) The schematics of four block layers with the detailed structural parameters as follows: $h = 5$ mm, $l = 2$ mm, $h_0 = 28$ mm, $a = 20$ mm, $d = 4.25$ mm, and $w = r = 1.5$ mm. (d) The bulk BZ and (e) band dispersion along the high-symmetry lines.

Utilizing cylinders to connect the cavities of the layers, providing access to both nearest-neighbor and next-nearest-neighbor couplings, draws upon the advantageous design inherited from Refs. [30,65,86,87]. All of the numerical simulations are performed by employing the acoustic module of COMSOL MULTIPHYSICS and the detailed computational information is appended in the Supplemental Material (SM) [88].

We calculate the bulk dispersion of the unit cell, as displayed in Fig. 2(e), where BZ is displayed in Fig. 2(d). Clearly, a twofold degenerate point (labeled by a blue sphere) at Γ exhibits a quadratic dispersion in the k_x-k_y plane and a linear dispersion in the k_z direction, whereas two nodal surfaces protected by $\mathcal{T}S_{2i}(i = x, y, z)$ meet at A to form a fourfold degenerate point (labeled by a red sphere) with linear dispersion in all three directions, which is compatible with our analysis of the $k \cdot p$ model. Next is the revelation that the node at Γ carries a topological charge of $+2$, while the node at A holds a topological charge of -2, which are the spotlight of our discussion. In fact, the widely adopted method [53,65,89] to verify the number and sign of topological charges of a node involves monitoring the quantity and trend of the gapless surface states generated by the projected bulk dispersion bands. In Fig. 3(a), two cylinders within the BZ are selected to wrap around Γ (marked blue) and A (marked red), with the corresponding projections along the (001) direction represented by a blue circle encircling the $\overline{\Gamma}$ point and a red circle encircling the $\overline{\mathrm{A}}$ point. Considering the bulk-edge correspondence, the surface dispersion bands along the projected loop provide insights into the topological charges of the nodes within the cylinder. Here, we employ a $1 \times 1 \times 20$ cell with open boundary in the z direction and periodic boundaries in the x and y directions. Specifically illustrated in Fig. 3(b), the two chiral states ranging from low to high frequencies in the projected dispersion bands of the blue loop around the $\overline{\Gamma}$ point reveal that the twofold degenerate point at Γ carries a topological charge of $+2$, viz., a charge-2 WP. Following a similar procedure, the two chiral states around the $\overline{\mathrm{A}}$ point exhibiting an opposite slope in Fig. 3(c) indicate that the

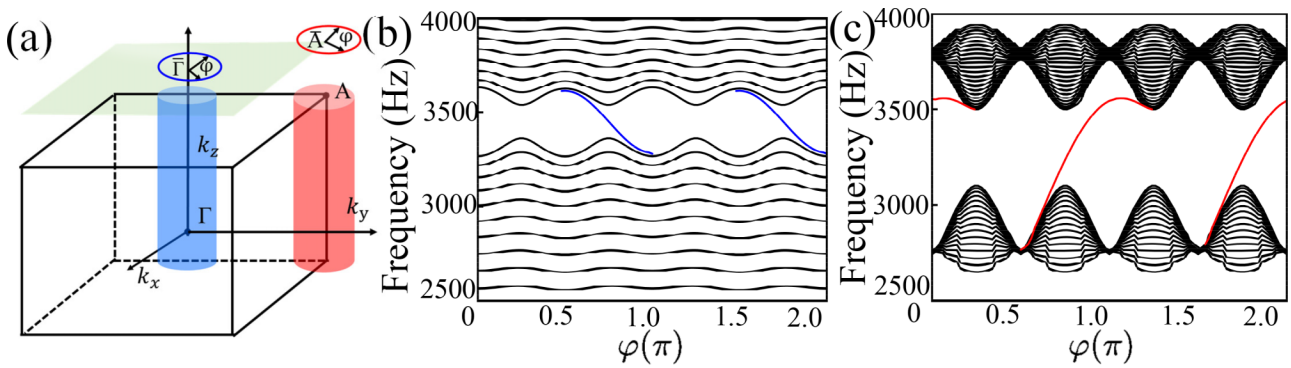

FIG. 3. (a) Cylinders around the points Γ and A with the baselines on the projected BZs, where the radius of the blue and red circles are $0.4\,\pi/a$. Projected band dispersions along the circular path φ for (b) $\overline{\Gamma}$ and (c) $\overline{\mathrm{A}}$.

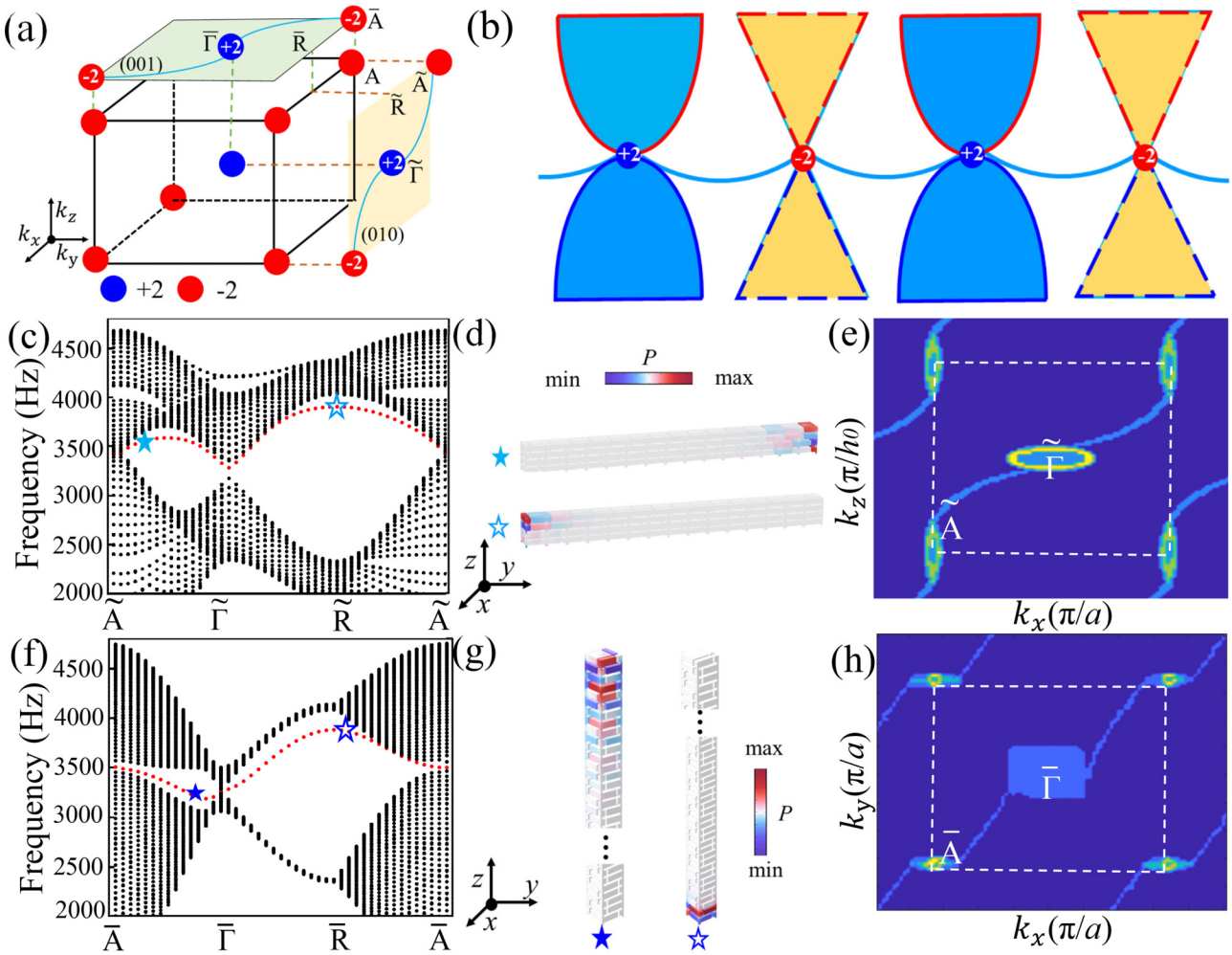

FIG. 4. (a) Schematic illustration of a charge-2 WP (blue sphere with topological charge = +2) and a charge-2 DP (red sphere with topological charge = −2) at bulk BZ with surface arcs projected on the (010) and (001) surface BZs, featuring (b) the ultralong surface arc in the whole momentum space formed by the system of UDWS. Projected bulk dispersions along the high symmetry lines of the (c) (010) and (f) (001) projected surface BZs. The black solid lines are the projections of bulk bands; the red solid lines indicate the existence of topological surface states. (d) [(g)] Eigenmodes of the surface arc states at specific positions denoted by stars in (c) [(f)]. The isofrequency contours at the frequency of 3335 Hz projected on the (e) (010) and (h) (001) surfaces.

fourfold degenerate point at A is a charge-2 DP with a topological charge of −2. Further, our detailed check of the bulk dispersion bands confirms the absence of any additional degenerate points other than those identified at Γ and A points near a specific frequency, as the introduction of additional nodes might complicate the interpretation of the observed properties. Right now, we can confidently claim that the UDWS system containing only a charge-2 WP and a charge-2 DP is realized, where both nodes carry opposite topological charges that align with the principle of topological charge conservation. Such a concise system, embodying the ethos of minimalism in physics, implies that the topological surface modes of UDWS are not covered by the bulk modes and should be as clearly visible as possible to facilitate experimental detection. That is, the system is represented as an optimal platform for investigating the topological properties of UDWS. In addition, the SG 96 ($P4_32_12$) also satisfies the above constraints and is capable of carrying UDWS. Compared to the SG 92, the two are mutually enantiomorphic space groups [90] that are a mirror reflection relation, so we continue to employ SG 92 as a paradigm to observe UDWS.

A typical symbol of excitation of a node possessing topological charge is the emergence of the topologically protected surface arc, which terminates at the projection point of the node on the surface BZ in the projection direction. Notably, the concise UDWS system features a nodal distribution with a charge-2 DP at the boundary of a BZ and a charge-2 WP at the center of a BZ. When considering the (010) direction, the projection of Γ and A points onto the central and boundary points of the surface BZ are denoted as $\widetilde{\Gamma}$ and $\widetilde{\mathrm{A}}$ points, respectively. Accounting for the constraints of topological charge conservation, the surface arcs facilitate the establishment of a connection pattern of $\widetilde{\mathrm{A}}$-$\widetilde{\Gamma}$-$\widetilde{\mathrm{A}}$, as visually illustrated in Fig. 4(a). Additionally, the distinctive distribution characteristics of the nodal structure tend to extend preferentially into the neighboring Brillouin zone, leading to the formation of an ultralong surface arc that spans the entire BZ, as depicted in Fig. 4(b). This characteristic enables easier observation

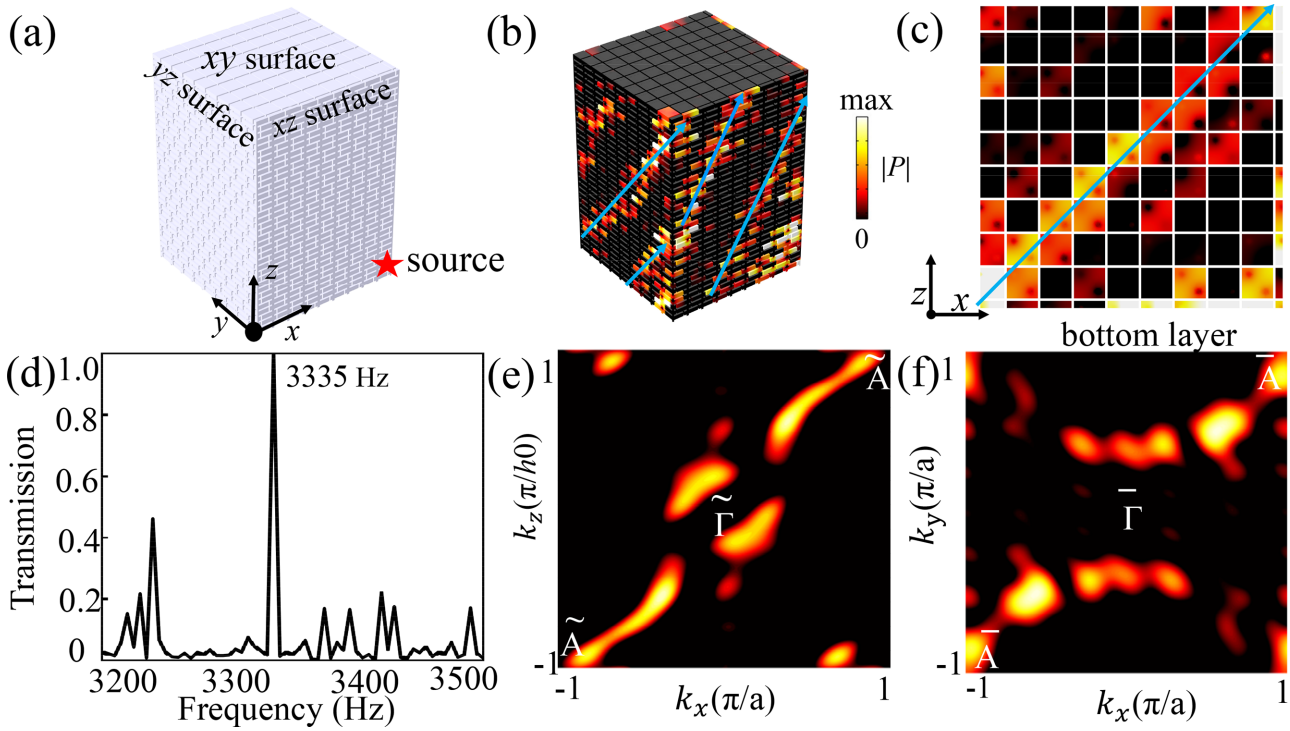

FIG. 5. (a) Schematic of the acoustic model comprising $9 \times 9 \times 9$ cells. The red star represents the source position. (b) Simulated pressure amplitude distribution of acoustic waves on the surface at 3335 Hz. (c) Pressure amplitude distribution on the bottom xy surface, where the cyan arrows represent the direction of wave propagation. (d) Simulated transmission spectrum of acoustic surface modes propagating in the y direction. (e), (f) The calculated surface isofrequency contours by Fourier transforming the pressure fields on (010) and (001) surfaces at 3375 Hz and 3305 Hz, respectively.

and manipulation compared to the paired WPs with a shorter surface arc confined within the BZ. The significance of this attribute is confirmed by the clear presence of red stripes in the projected dispersion bands, as shown in Fig. 4(c). Furthermore, Fig. 4(d) shows the two eigenmodes for the marked frequency, exhibiting their localized behavior and confirming the red stripes as boundary states. Examining the isofrequency contours in Fig. 4(e), we visualize the double helical surface arcs following the $\tilde{A}$-$\tilde{\Gamma}$-$\tilde{A}$ route and extending into the neighboring BZ, showcasing an ultralong trajectory feature. Similarly, in the (001) direction, ultralong surface arcs linking the projection points $\bar{A}$-$\bar{\Gamma}$-$\bar{A}$ can also be identified, visualized through the projected dispersion bands in Fig. 4(f), the field map in Fig. 4(g), and the isofrequency contour in Fig. 4(h). That is, the system is an ideal scheme due to the fact that it exhibits remarkable observational clarity surface patterns and can be distinguished from bulk modes. Moreover, under the influence of $\tilde{C}_4$ symmetry, the (010) and (100) directions are equivalent, implying that the topological surface states of the UDWS are not limited by projection surfaces, thus bolstering the feasibility and effectiveness of observations. In addition, by considering scenarios where the degenerate points exist on the high symmetry line with potential topological effects, we show all the possible schemes for space groups that support UDWS in SM [88].

Next, we investigate the surface response of the UDWS within the finite system. As depicted in Fig. 5(a), the mode comprised $9 \times 9 \times 9$ cells, with an source positioned at the bottom marked by a red star to excite the Bloch states. The pressure distribution field in Fig. 5(b) demonstrates the remarkable propagation capability of the surface states. Notably, the propagation direction is approximately diagonal to the x-z and y-z planes, as evidenced by an additional diagram on the bottom of the x-z plane, as depicted in Fig. 5(c). This diagonal propagation is effectively understood through the isofrequency contours derived from the Fourier-transformed pressure field. The outcomes reveal the establishment of $\tilde{A}$-$\tilde{\Gamma}$-$\tilde{A}$ pathways in the (010) direction [as depicted in Fig. 5(e)] and $\bar{A}$-$\bar{\Gamma}$-$\bar{A}$ connections in the (001) direction [as illustrated in Fig. 5(f)], consistent with the findings in Figs. 4(e) and 4(h) of the one-dimensional finite structure. Furthermore, from numerical simulations, we can obtain the transmission of the acoustic boundary mode in the y direction in Fig. 5(d), highlighting a distinctive peak at 3335 Hz, validating the transmission efficiency of UDWS in information propagation.

The investigation of the robustness of surface states against defects and sharp bends in finite systems is imperative. We examine a defective structure comprising 3×3 cells, which manifests its two ways of adding and removing into the x-z plane in a finite $7 \times 7 \times 10$ model, as shown in Figs. 6(a) and 6(d), respectively. At the bottom corner, a source is positioned and marked by a red star. The field diagrams in two defective configurations [see in Figs. 6(b) and 6(d)] show that the surface state of UDWS involves immunity against two defects. Cross-sectional views at $x = 4.5a$ within the defect region, as a bolster instruction in Figs. 6(c) and 6(f), demonstrate that the surface wave circumvents the defect region and propagates

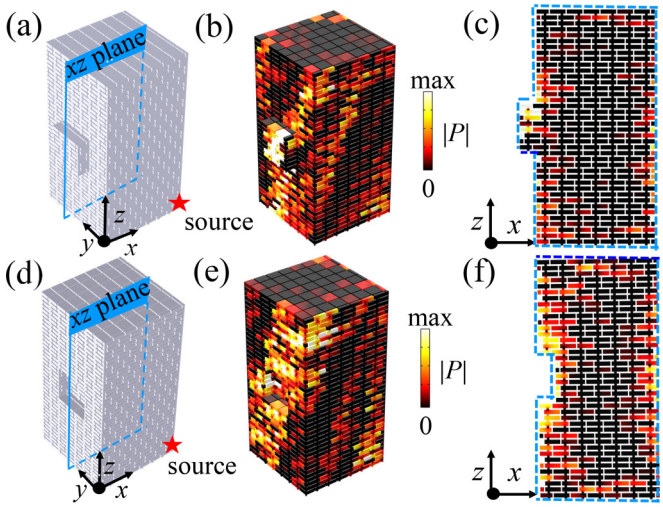

FIG. 6. Robustness of the topological surface states. (a) A schematic of defective UDWS with a $7 \times 7 \times 10$ supercell. The defect configuration involves the addition of 3×3 cells at the center of the y-z plane. The red star denotes the location of the acoustic source, showcasing (b) simulated bulk field distribution and (c) the cross sections of the x-z plane at $y = 4.5a$ for a frequency of 3370 Hz with cyan dotted lines to outline the boundaries. (d)–(f) Similarly illustrated as in (a)–(c), but for a simulated sample featuring another defective UDWS created by removing 3×3 cells at the center of the y-z plane.

along the boundary, confirming the robustness of the surface state of UDWS.

IV. CONCLUSIONS

In conclusion, we successfully achieve a unique single UDWS in a phononic crystal. In detail, the single-paired system reveals that charge-2 WP and charge-2 DP occupy separate high-symmetry points with symmetry protection. We construct a phononic crystal confirming that the single UDWS has a double helical surface arc, showing ultralong properties through the entire surface of the BZ. This unique global surface connectivity provides conclusive evidence for a "real" connection established between the two types of unconventional nodes in our UDWS system. Our system not only provides special advantages for exploring the association between the charge-2 DP and charge-2 WP but also paves the way for potential applications in nontrivial transmission channels of acoustic devices, such as waveguides and splitters. Moreover, the ultralong surface arcs can be further extended to other fields, such as photonic crystals, mechanical systems, and cold atom systems.

ACKNOWLEDGMENT

This work was financially supported by the National Key Research and Development Program of China (No. 2023YFB4604800).

[1] X. G. Wan, A. M. Turner, A. Vishwanath, and S. Y. Savrasov, Topological semimetal and Fermi-arc surface states in the electronic structure of pyrochlore iridates, Phys. Rev. B **83**, 205101 (2011).

[2] B. Q. Lv, S. Muff, T. Qian, Z. D. Song, S. M. Nie, N. Xu, P. Richard, C. E. Matt, N. C. Plumb, L. X. Zhao, G. F. Chen, Z. Fang, X. Dai, J. H. Dil, J. Mesot, M. Shi, H. M. Weng, and H. Ding, Observation of Fermi-arc spin texture in TaAs, Phys. Rev. Lett. **115**, 217601 (2015).

[3] H. M. Weng, C. Fang, Z. Fang, B. A. Bernevig, and X. Dai, Weyl semimetal phase in noncentrosymmetric transition-metal monophosphides, Phys. Rev. X **5**, 011029 (2015).

[4] A. A. Soluyanov, D. Gresch, Z. Wang, Q. S. Wu, M. Troyer, X. Dai, and B. A. Bernevig, Type-II Weyl semimetals, Nature (London) **527**, 495 (2015).

[5] P. Tang, Q. Zhou, and S.-C. Zhang, Multiple types of topological fermions in transition metal silicides, Phys. Rev. Lett. **119**, 206402 (2017).

[6] M. Yan, X. Q. Huang, J. Wu, W. Y. Deng, J. Y. Lu, and Z. Y. Liu, Antichirality emergent in type-II Weyl phononic crystals, Phys. Rev. Lett. **130**, 266304 (2023).

[7] X. Q. Huang, W. Y. Deng, F. Li, J. Y. Lu, and Z. Y. Liu, Ideal type-II weyl phase and topological transition in phononic crystals, Phys. Rev. Lett. **124**, 206802 (2020).

[8] D. T. Son and B. Z. Spivak, Chiral anomaly and classical negative magnetoresistance of Weyl metals, Phys. Rev. B **88**, 104412 (2013).

[9] J. Cano, B. Bradlyn, Z. Wang, M. Hirschberger, N. P. Ong, and B. A. Bernevig, Chiral anomaly factory: Creating Weyl fermions with a magnetic field, Phys. Rev. B **95**, 161306(R) (2017).

[10] A. A. Zyuzin and A. A. Burkov, Topological response in Weyl semimetals and the chiral anomaly, Phys. Rev. B **86**, 115133 (2012).

[11] M. M. Vazifeh and M. Franz, Electromagnetic response of Weyl semimetals, Phys. Rev. Lett. **111**, 027201 (2013).

[12] X. C. Huang, L. X. Zhao, Y. J. Long, P. P. Wang, D. Chen, Z. H. Yang, H. Liang, M. Q. Xue, H. M. Weng, Z. Fang, X. Dai, and G. Chen, Observation of the chiral-anomaly-induced negative magnetoresistance in 3D Weyl semimetal TaAs, Phys. Rev. X **5**, 031023 (2015).

[13] S. A. Parameswaran, T. Grover, D. A. Abanin, D. A. Pesin, and A. Vishwanath, Probing the chiral anomaly with nonlocal transport in three-dimensional topological semimetals, Phys. Rev. X **4**, 031035 (2014).

[14] C.-X. Liu, P. Ye, and X.-L. Qi, Chiral gauge field and axial anomaly in a Weyl semimetal, Phys. Rev. B **87**, 235306 (2013).

[15] Z. Wang, H. Weng, Q. Wu, X. Dai, and Z. Fang, Three-dimensional Dirac semimetal and quantum transport in Cd_3As_2, Phys. Rev. B **88**, 125427 (2013).

[16] M. Milićević, G. Montambaux, T. Ozawa, O. Jamadi, B. Real, I. Sagnes, A. Lemaître, L. Le Gratiet, A. Harouri, J. Bloch, and A. Amo, Type-III and tilted Dirac cones emerging from flat bands in photonic orbital graphene, Phys. Rev. X **9**, 031010 (2019).

[17] X. X. Wu, X. Li, R.-Y. Zhang, X. Xiang, J. X. Tian, Y. Z. Huang, S. X. Wang, B. Hou, C. T. Chan, and W. J. Wen, Deterministic scheme for two-dimensional type-II Dirac points

and experimental realization in acoustics, Phys. Rev. Lett. **124**, 075501 (2020).

[18] L. Y. Yang, Y. Wang, Y. Meng, Z. X. Zhu, X. Xi, B. Yan, S. X. Lin, J. M. Chen, B.-J. Shi, Y. Ge, S.-Q. Yuan, H. S. Chen, H.-X. Sun, G.-G. Liu, Y. H. Yang, and Z. Gao, Observation of Dirac hierarchy in three-dimensional acoustic topological insulators, Phys. Rev. Lett. **129**, 125502 (2022).

[19] X. X. Cai, L. P. Ye, C. Y. Qiu, M. Xiao, R. Yu, M. Z. Ke, and Z. Y. Liu, Symmetry-enforced three-dimensional Dirac phononic crystals, Light Sci. Appl. **9**, 38 (2020).

[20] Z. J. Chen, R. Wang, B. W. Xia, B. B. Zheng, Y. J. Jin, Y.-J. Zhao, and H. Xu, Three-dimensional Dirac phonons with inversion symmetry, Phys. Rev. Lett. **126**, 185301 (2021).

[21] G.-G. Liu, P. H. Zhou, Y. H. Yang, H. R. Xue, X. Ren, X. Lin, H.-X. Sun, L. Bi, Y. D. Chong, and B. L. Zhang, Observation of an unpaired photonic Dirac point, Nat. Commun. **11**, 1873 (2020).

[22] Z. J. Wang, Y. Sun, X.-Q. Chen, C. Franchini, G. Xu, H. M. Weng, X. Dai, and Z. Fang, Dirac semimetal and topological phase transitions in A_3Bi (A=Na, K, Rb), Phys. Rev. B **85**, 195320 (2012).

[23] S. M. Young, S. Zaheer, J. C. Y. Teo, C. L. Kane, E. J. Mele, and A. M. Rappe, Dirac semimetal in three dimensions, Phys. Rev. Lett. **108**, 140405 (2012).

[24] T. Liang, Q. Gibson, M. N. Ali, M. Liu, R. J. Cava, and N. P. Ong, Ultrahigh mobility and giant magnetoresistance in the Dirac semimetal Cd_3As_2, Nat. Mater. **14**, 280 (2015).

[25] C. Fang, M. J. Gilbert, X. Dai, and B. A. Bernevig, Multi-Weyl topological semimetals stabilized by point group symmetry, Phys. Rev. Lett. **108**, 266802 (2012).

[26] G. Xu, H. M. Weng, Z. J. Wang, X. Dai, and Z. Fang, Chern semimetal and the quantized anomalous Hall effect in $HgCr_2Se_4$, Phys. Rev. Lett. **107**, 186806 (2011).

[27] Z. M. Zhu, G. W. Winkler, Q. S. Wu, J. Li, and A. A. Soluyanov, Triple point topological metals, Phys. Rev. X **6**, 031003 (2016).

[28] S. Singh, Q. S. Wu, C. Yue, A. H. Romero, and A. A. Soluyanov, Topological phonons and thermoelectricity in triple-point metals, Phys. Rev. Mater. **2**, 114204 (2018).

[29] G. W. Winkler, S. Singh, and A. A. Soluyanov, Topology of triple-point metals*, Chin. Phys. B **28**, 077303 (2019).

[30] X. Shi and J. Yang, Spin-1 Weyl point and surface arc state in a chiral phononic crystal, Phys. Rev. B **101**, 214309 (2020).

[31] G. Q. Chang, S.-Y. Xu, B. J. Wieder, D. S. Sanchez, S.-M. Huang, I. Belopolski, T.-R. Chang, S. Zhang, A. Bansil, H. Lin, and M. Z. Hasan, Unconventional chiral fermions and large topological Fermi arcs in RhSi, Phys. Rev. Lett. **119**, 206401 (2017).

[32] D. Takane, Z. Wang, S. Souma, K. Nakayama, T. Nakamura, H. Oinuma, Y. Nakata, H. Iwasawa, C. Cacho, T. Kim, K. Horiba, H. Kumigashira, T. Takahashi, Y. Ando, and T. Sato, Observation of chiral fermions with a large topological charge and associated Fermi-arc surface states in CoSi, Phys. Rev. Lett. **122**, 076402 (2019).

[33] H. Miao, T. T. Zhang, L. Wang, D. Meyers, A. H. Said, Y. L. Wang, Y. G. Shi, H. M. Weng, Z. Fang, and M. P. M. Dean, Observation of double Weyl phonons in parity-breaking FeSi, Phys. Rev. Lett. **121**, 035302 (2018).

[34] T. T. Zhang, Z. D. Song, A. Alexandradinata, H. M. Weng, C. Fang, L. Lu, and Z. Fang, Double-Weyl phonons in transition-metal monosilicides, Phys. Rev. Lett. **120**, 016401 (2018).

[35] H. L. He, Z. H. Pu, Q. Y. Ma, Z. Dong, L. P. Ye, M. Z. Ke, and Z. Y. Liu, Excitation of maximal degeneracy and higher-order topology in phononic crystals, Phys. Rev. Appl. **20**, 064034 (2023).

[36] S. Nie, B. A. Bernevig, and Z. Wang, Sixfold excitations in electrides, Phys. Rev. Res. **3**, L012028 (2021).

[37] C. W. Xie, Y. Liu, Z. Y. Zhang, F. Zhou, T. Yang, M. Q. Kuang, X. T. Wang, and G. Zhang, Sixfold degenerate nodal-point phonons: Symmetry analysis and materials realization, Phys. Rev. B **104**, 045148 (2021).

[38] T. Bzdušek, Q. Wu, A. Rüegg, M. Sigrist, and A. A. Soluyanov, Nodal-chain metals, Nature (London) **538**, 75 (2016).

[39] J. Y. Lu, X. Q. Huang, M. Yan, F. Li, W. Y. Deng, and Z. Y. Liu, Nodal-chain semimetal states and topological focusing in phononic crystals, Phys. Rev. Appl. **13**, 054080 (2020).

[40] H. H. Qiu, Q. C. Zhang, T. Z. Liu, X. Y. Fan, and C. Y. Qiu, Observation of fourfold nodal hinges and toruslike surface modes in acoustic metamaterials, Phys. Rev. B **108**, L201102 (2023).

[41] H. Qiu, C. Qiu, R. Yu, M. Xiao, H. He, L. Ye, M. Ke, and Z. Liu, Straight nodal lines and waterslide surface states observed in acoustic metacrystals, Phys. Rev. B **100**, 041303(R) (2019).

[42] R. Yu, H. M. Weng, Z. Fang, X. Dai, and X. Hu, Topological node-line semimetal and Dirac semimetal state in antiperovskite Cu_3PdN, Phys. Rev. Lett. **115**, 036807 (2015).

[43] M. Kim, D. Lee, D. Lee, and J. Rho, Topologically nontrivial photonic nodal surface in a photonic metamaterial, Phys. Rev. B **99**, 235423 (2019).

[44] Y. H. Yang, J.-p. Xia, H.-x. Sun, Y. Ge, D. Jia, S.-q. Yuan, S. A. Yang, Y. D. Chong, and B. L. Zhang, Observation of a topological nodal surface and its surface-state arcs in an artificial acoustic crystal, Nat. Commun. **10**, 5185 (2019).

[45] M. Xiao, L. P. Ye, C. Y. Qiu, H. L. He, Z. Y. Liu, and S. H. Fan, Experimental demonstration of acoustic semimetal with topologically charged nodal surface, Sci. Adv. **6**, eaav2360 (2020).

[46] W. K. Wu, Y. Liu, S. Li, C. Y. Zhong, Z.-M. Yu, X.-L. Sheng, Y. X. Zhao, and S. A. Yang, Nodal surface semimetals: Theory and material realization, Phys. Rev. B **97**, 115125 (2018).

[47] F. Gao, Y.-G. Peng, X. Xiang, Q.-L. Sun, C. Zheng, B. Li, and X.-F. Zhu, Visualization of orbital twig edge states in phononic graphene lattices, Phys. Rev. Appl. **21**, 044005 (2024).

[48] F. Gao, Y.-G. Peng, Q.-L. Sun, X. Xiang, C. Zheng, and X.-F. Zhu, Topological acoustics with orbital-dependent gauge fields, Phys. Rev. Appl. **20**, 064036 (2023).

[49] Q.-L. Sun, Y.-G. Peng, F. Gao, B. Li, and X.-F. Zhu, Montage operation of plaquette states in acoustic orbital lattices with type-III Dirac points, Phys. Rev. Appl. **20**, 024025 (2023).

[50] Y.-X. Shen, Y.-G. Peng, P.-C. Cao, J. Li, and X.-F. Zhu, Observing localization and delocalization of the flat-band states in an acoustic cubic lattice, Phys. Rev. B **105**, 104102 (2022).

[51] Y. J. Ding, Y.-G. Peng, Y. F. Zhu, X. D. Fan, J. Yang, B. Liang, X.-F. Zhu, X. G. Wan, and J. C. Cheng, Experimental demonstration of acoustic Chern insulators, Phys. Rev. Lett. **122**, 014302 (2019).

[52] P. T. Lai, H. Liu, B. Y. Xie, W. Y. Deng, H. N. Wang, H. Cheng, Z. Y. Liu, and S. Q. Chen, Spin Chern insulator in a phononic fractal lattice, Phys. Rev. B **109**, L140104 (2024).

[53] W. Y. Deng, X. Q. Huang, J. Y. Lu, F. Li, J. H. Ma, S. Q. Chen, and Z. Y. Liu, Acoustic spin-1 Weyl semimetal, Sci. China Phys. Mech. Astron. **63**, 287032 (2020).

[54] Y. J. Qi, C. Y. Qiu, M. Xiao, H. L. He, M. Z. Ke, and Z. Y. Liu, Acoustic realization of quadrupole topological insulators, Phys. Rev. Lett. **124**, 206601 (2020).

[55] L. P. Ye, Q. Y. Ma, S. D. Yin, D. Yao, H. L. He, M. Z. Ke, and Z. Y. Liu, Acoustic quadrupolar surface topological semimetals, Phys. Rev. Appl. **19**, 064064 (2023).

[56] Y. H. Yang, Z. Gao, X. L. Feng, Y.-X. Huang, P. H. Zhou, S. A. Yang, Y. D. Chong, and B. L. Zhang, Ideal unconventional Weyl point in a chiral photonic metamaterial, Phys. Rev. Lett. **125**, 143001 (2020).

[57] H. L. He, C. Y. Qiu, X. X. Cai, M. Xiao, M. Z. Ke, F. Zhang, and Z. Y. Liu, Observation of quadratic Weyl points and double-helicoid arcs, Nat. Commun. **11**, 1820 (2020).

[58] Y. H. Yang, H.-X. Sun, J.-P. Xia, H. R. Xue, Z. Gao, Y. Ge, D. Jia, S.-Q. Yuan, Y. D. Chong, and B. L. Zhang, Topological triply degenerate point with double Fermi arcs, Nat. Phys. **15**, 645 (2019).

[59] Z. H. Pu, H. L. He, L. C. Luo, Q. Y. Ma, L. P. Ye, M. Z. Ke, and Z. Y. Liu, Acoustic higher-order Weyl semimetal with bound hinge states in the continuum, Phys. Rev. Lett. **130**, 116103 (2023).

[60] X. Xiang, Y.-G. Peng, F. Gao, X. X. Wu, P. Wu, Z. X. Chen, X. Ni, and X.-F. Zhu, Demonstration of acoustic higher-order topological Stiefel-Whitney semimetal, Phys. Rev. Lett. **132**, 197202 (2024).

[61] H. H. Qiu, Y. Z. Li, Q. C. Zhang, and C. Y. Qiu, Discovery of higher-order nodal surface semimetals, Phys. Rev. Lett. **132**, 186601 (2024).

[62] F. Gao, X. Xiang, Y.-G. Peng, X. Ni, Q.-L. Sun, S. Yves, X.-F. Zhu, and A. Alù, Orbital topological edge states and phase transitions in one-dimensional acoustic resonator chains, Nat. Commun. **14**, 8162 (2023).

[63] H. L. He, C. Y. Qiu, L. P. Ye, X. X. Cai, X. Y. Fan, M. Z. Ke, F. Zhang, and Z. Y. Liu, Topological negative refraction of surface acoustic waves in a Weyl phononic crystal, Nature (London) **560**, 61 (2018).

[64] Y. C. Liu, G. P. Wang, J. B. Pendry, and S. Zhang, All-angle reflectionless negative refraction with ideal photonic Weyl metamaterials, Light Sci. Appl. **11**, 276 (2022).

[65] R. Y. Zheng, Y. T. Yang, W. Y. Deng, J. Y. Lu, X. Q. Huang, and Z. Y. Liu, Quadratic Weyl semimetal and topological double negative refraction in phononic crystals, Phys. Rev. Appl. **20**, 044035 (2023).

[66] S. A. R. Horsley and M. Woolley, Zero-refractive-index materials and topological photonics, Nat. Phys. **17**, 348 (2021).

[67] T. Z. Xia, Y. Z. Li, Q. C. Zhang, X. Y. Fan, M. Xiao, and C. Y. Qiu, Observation of hybrid-order topological pump in a kekulé-textured graphene lattice, Phys. Rev. B **108**, 125125 (2023).

[68] D. Y. Wang, H. W. Jia, Q. L. Yang, J. Hu, Z. Q. Zhang, and C. T. Chan, Intrinsic triple degeneracy point bounded by nodal surfaces in chiral photonic crystal, Phys. Rev. Lett. **130**, 203802 (2023).

[69] M. D. Wang, R.-Y. Zhang, L. Zhang, D. Y. Wang, Q. H. Guo, Z.-Q. Zhang, and C. T. Chan, Topological one-way large-area waveguide states in magnetic photonic crystals, Phys. Rev. Lett. **126**, 067401 (2021).

[70] G.-G. Liu, Z. Gao, Q. Wang, X. Xi, Y.-H. Hu, M. Wang, C. Liu, X. Lin, L. J. Deng, S. A. Yang, P. H. Zhou, Y. H. Yang, Y. D. Chong, and B. L. Zhang, Topological Chern vectors in three-dimensional photonic crystals, Nature (London) **609**, 925 (2022).

[71] F. de Juan, A. G. Grushin, T. Morimoto, and J. E. Moore, Quantized circular photogalvanic effect in Weyl semimetals, Nat. Commun. **8**, 15995 (2017).

[72] G. Q. Chang, J.-X. Yin, T. Neupert, D. S. Sanchez, I. Belopolski, S. S. Zhang, T. A. Cochran, Z. Chéng, M.-C. Hsu, S.-M. Huang, B. Lian, S.-Y. Xu, H. Lin, and M. Z. Hasan, Unconventional photocurrents from surface Fermi arcs in topological chiral semimetals, Phys. Rev. Lett. **124**, 166404 (2020).

[73] Z. H. Gao, M. Hua, H. J. Zhang, and X. Zhang, Classification of stable Dirac and Weyl semimetals with reflection and rotational symmetry, Phys. Rev. B **93**, 205109 (2016).

[74] Z. K. Liu, B. Zhou, Y. Zhang, Z. J. Wang, H. M. Weng, D. Prabhakaran, S.-K. Mo, Z. X. Shen, Z. Fang, X. Dai, Z. Hussain, and Y. L. Chen, Discovery of a three-dimensional topological Dirac semimetal Na_3Bi, Science **343**, 864 (2014).

[75] S. Long, J. Yang, H. Wang, Z. Yu, B. Yang, Q. Guo, Y. Xiang, L. Xia, and S. Zhang, Dirac–Weyl semimetal in photonic metacrystals, Opt. Lett. **48**, 2349 (2023).

[76] H. Gao, Y. Kim, J. W. F. Venderbos, C. L. Kane, E. J. Mele, A. M. Rappe, and W. Ren, Dirac-Weyl semimetal: Coexistence of Dirac and Weyl fermions in polar hexagonal *ABC* crystals, Phys. Rev. Lett. **121**, 106404 (2018).

[77] A. Furusaki, Weyl points and Dirac lines protected by multiple screw rotations, Sci. Bull. **62**, 788 (2017).

[78] J. H. Wang, H. K. Yuan, Y. Liu, F. Zhou, X. T. Wang, and G. Zhang, Hourglass Weyl and Dirac nodal line phonons and drumhead-like and torus phonon surface states in orthorhombic-type KCuS, Phys. Chem. Chem. Phys. **24**, 2752 (2022).

[79] Y. Xu and C. W. Zhang, Dirac and Weyl rings in three-dimensional cold-atom optical lattices, Phys. Rev. A **93**, 063606 (2016).

[80] J. H. Wang, H. K. Yuan, Z.-M. Yu, Z. Y. Zhang, and X. T. Wang, Coexistence of symmetry-enforced phononic Dirac nodal-line net and three-nodal surfaces phonons in solid-state materials: Theory and materials realization, Phys. Rev. Mater. **5**, 124203 (2021).

[81] Z.-M. Wang, R. Wang, J.-H. Sun, T.-Y. Chen, and D.-H. Xu, Floquet Weyl semimetal phases in light-irradiated higher-order topological Dirac semimetals, Phys. Rev. B **107**, L121407 (2023).

[82] R. Wang, B. W. Xia, Z. J. Chen, B. B. Zheng, Y. J. Zhao, and H. Xu, Symmetry-protected topological triangular Weyl complex, Phys. Rev. Lett. **124**, 105303 (2020).

[83] M. I. Aroyo, J. M. Perez-Mato, D. Orobengoa, E. Tasci, G. de la Flor, and A. Kirov, Crystallography online: Bilbao crystallographic server, Bulg. Chem. Commun. **43**, 183 (2011).

[84] A. A. Soluyanov and D. Vanderbilt, Computing topological invariants without inversion symmetry, Phys. Rev. B **83**, 235401 (2011).

[85] R. Yu, X. L. Qi, A. Bernevig, Z. Fang, and X. Dai, Equivalent expression of $\mathcal{Z}_2$ topological invariant for band insulators using the non-Abelian Berry connection, Phys. Rev. B **84**, 075119 (2011).

[86] H.-X. Wang, Z.-K. Lin, B. Jiang, G.-Y. Guo, and J.-H. Jiang, Higher-order Weyl semimetals, Phys. Rev. Lett. **125**, 146401 (2020).

[87] L. Luo, H.-X. Wang, Z.-K. Lin, B. Jiang, Y. Wu, F. Li, and J.-H. Jiang, Observation of a phononic higher-order Weyl semimetal, Nat. Mater. **20**, 794 (2021).

[88] See Supplemental Material at http://link.aps.org/supplemental/10.1103/PhysRevB.110.094104 for the other possible schemes for the UDWS phase and the recipes for simulation.

[89] Z.-Q. Wang, Q.-B. Liu, X.-F. Yang, and H.-H. Fu, Single-pair Weyl points with the maximum charge number in acoustic crystals, Phys. Rev. B **106**, L161302 (2022).

[90] M. J. Mehl, D. Hicks, C. Toher, O. Levy, R. M. Hanson, G. Hart, and S. Curtarolo, The aflow library of crystallographic prototypes: Part 1, Comput. Mater. Sci. **136**, S1 (2017).